Mon. Not. R. Astron. Soc. **000**, 1–17 (2013) Printed 1 July 2013 (MN LATEX style file v2.2)

Unveiling the corona of the Milky Way via ram-pressure stripping of dwarf satellites

A. Gatto,[1,2⋆] F. Fraternali,[2,3] J. I. Read,[4] F. Marinacci,[5,6] H. Lux[7,8] and S. Walch[1]
[1] *Max-Planck Institute for Astrophysics, Karl-Schwarzschild Strasse 1, D-85748 Garching, Germany*
[2] *Department of Physics and Astronomy, University of Bologna, via Berti Pichat 6/2, I-40127 Bologna, Italy*
[3] *Kapteyn Astronomical Institute, Postbus 800, NL-9700 AV, Groningen, The Netherlands*
[4] *University of Surrey, Guildford, Surrey GU2 7XH, UK*
[5] *Heidelberg Institute for Theoretical Studies, Schloss-Wolfsbrunnenweg 35, D-69118 Heidelberg, Germany*
[6] *Center for Astronomy of Heidelberg University, Astronomisches Recheninstitut, Mönchhfstr. 12-14, D-69120 Heidelberg, Germany*
[7] *School of Physics and Astronomy, University of Nottingham, University Park, Nottingham NG7 2RD, UK*
[8] *Department of Physics, University of Oxford, Denys Wilkinson Building, Keble Road, Oxford OX1 3RH, UK*

Accepted 2013 May 17. Received 2013 May 16; in original form 2013 February 25

ABSTRACT
The spatial segregation between dwarf spheroidal (dSph) and dwarf irregular galaxies in the Local Group has long been regarded as evidence of an interaction with their host galaxies. In this paper, we assume that ram-pressure stripping is the dominant mechanism that removed gas from the dSphs and we use this to derive a lower bound on the density of the corona of the Milky Way at large distances ($R \sim 50 - 90\,\mathrm{kpc}$) from the Galactic Centre. At the same time, we derive an upper bound by demanding that the interstellar medium of the dSphs is in pressure equilibrium with the hot corona. We consider two dwarfs (Sextans and Carina) with well-determined orbits and star formation histories. Our approach introduces several novel features: (i) we use the measured star formation histories of the dwarfs to derive the time at which they last lost their gas, and (via a modified version of the Kennicutt-Schmidt relation) their internal gas density at that time; (ii) we use a large suite of 2D hydrodynamical simulations to model the gas stripping; and (iii) we include supernova feedback tied to the gas content. Despite having very different orbits and star formation histories, we find results for the two dSphs that are in excellent agreement with one another. We derive an average particle density of the corona of the Milky Way at $R = 50 - 90\,\mathrm{kpc}$ in the range $n_{\rm cor} = 1.3 - 3.6 \times 10^{-4}\,\mathrm{cm}^{-3}$. Including additional constraints from X-ray emission limits and pulsar dispersion measurements (that strengthen our upper bound), we derive Galactic coronal density profiles. Extrapolating these to large radii, we estimate the fraction of baryons (missing baryons) that can exist within the virial radius of the Milky Way. For an isothermal corona ($T_{\rm cor} = 1.8 \times 10^6\,\mathrm{K}$), this is small – just $10 - 20\%$ of the expected missing baryon fraction, assuming a virial mass of $1 - 2 \times 10^{12}\,M_\odot$. Only a hot ($T_{\rm cor} = 3 \times 10^6\,\mathrm{K}$) and adiabatic corona can contain all of the Galaxy's missing baryons. Models for the Milky Way must explain why its corona is in a hot adiabatic thermal state; or why a large fraction of its baryons lie beyond the virial radius.

Key words: methods: numerical – Galaxy: evolution – Galaxy: halo – galaxies: dwarf – galaxies: evolution – galaxies: ISM.

1 INTRODUCTION

In the current cosmological framework, the fraction of baryonic matter to dark matter (DM) is known to a high level of precision, thanks to both big-bang nucleosynthesis (Pagel 1997) and the study of the cosmic microwave background (e.g. Komatsu et al. 2009, Planck Collaboration 2013). By contrast, the fraction of baryons observed in the form of stars and gas in collapsed structures in the Universe is rather scant, which is commonly referred to as the *missing baryon problem*. Only massive galaxy clusters appear to have the amount of baryons expected, mostly in the form of hot gas that permeates their deep potential wells (e.g. Sarazin 2009). Galaxy groups and isolated galaxies contain a fraction of

⋆ e-mail: andreag@mpa-garching.mpg.de

detectable baryons which is a factor of ~ 10 smaller than the expected fraction and this discrepancy steadily increases with decreasing virial mass (e.g. Read & Trentham 2005; McGaugh et al. 2010).

Disc galaxies represent particularly challenging environments. Applying the cosmological baryon fraction to the virial mass of the Milky Way (MW; $1-2\times10^{12}\,\mathrm{M}_\odot$, e.g. Wilkinson & Evans 1999), one would predict a total baryonic mass for the Galaxy of $\sim 2-3\times10^{11}\,\mathrm{M}_\odot$. However, the currently detected mass in stars is $\sim 5\times10^{10}\,\mathrm{M}_\odot$ (Dehnen & Binney 1998) while interstellar matter accounts only for $< 1\times10^{10}\,\mathrm{M}_\odot$ (Binney & Merrifield 1998; Nakanishi & Sofue 2006). Therefore, $\sim 70-80\%$ of the MW's baryons are missing. Similar discrepancies are obtained for other disc galaxies of comparable mass (e.g. Read & Trentham 2005).

A commonly accepted solution to this incongruity is that galaxies should be embedded in massive atmospheres – *cosmological coronae* – of hot gas at temperatures of a few 10^6 K which contain most of the baryons associated with their potential wells (Fukugita & Peebles 2006). To date, the detection of these coronae has proven rather elusive since at this temperature and density (and assuming a low metallicity) the gas is unable to efficiently absorb or emit photons through metal lines or bremsstrahlung radiation (e.g. Sutherland & Dopita 1993). Some disc galaxies do show X-ray emission outside of their discs, but in most cases this is clearly associated with star formation and the presence of galactic winds (Strickland et al. 2004). In general, owing to contamination from the disc, an unambiguous detection of a cosmological corona is difficult in disc galaxies, unless hot gas is seen at large distances ($\gtrsim 10\,\mathrm{kpc}$) above or below the disc plane. A notable case is the massive galaxy NGC 5746 (Pedersen et al. 2006), where an early claim of an extended X-ray emitting corona was later attributed to an error in the background subtraction in the *Chandra* data (Rasmussen et al. 2009). This case alone demonstrates that these studies are at the limit of the capabilities of current X-ray facilities (Bregman 2007, but see also Hodges-Kluck & Bregman 2013; Li & Wang 2013).

In the MW, there are several indirect indications of the presence of a hot corona. The first evidence was pointed out by Spitzer soon after the discovery of clouds at high latitude as a medium capable of providing their pressure confinement (Spitzer 1956). Head-tail shapes of high-velocity clouds (HVCs) are also considered as evidence of an interaction between them and the corona (Putman et al. 2011). Unfortunately, all measured distances of HVCs are within 10 kpc from the plane of the disc (e.g. Wakker et al. 2008). Thus it is not clear whether they are probing the cosmological corona or simply extra-planar hot gas. A perhaps more relevant observation is the asymmetry between the leading and trailing arms of the Magellanic Stream (e.g. Putman et al. 2003), which is seen further out ($\sim 50\,\mathrm{kpc}$) and could result from ram-pressure stripping (see Guhathakurta & Reitzel 1998; Mastropietro et al. 2005; Diaz & Bekki 2012). Finally, X-ray spectra towards bright active galactic nuclei (AGN) show absorption features – in particular O VII, Ne IX, and O VIII – characteristic of a corona at $T\gtrsim10^6$ K. However, the poor velocity resolution of these spectra does not allow us to determine the extent of this medium and the current estimates range from a few kpc to ~ 1 Mpc (Nicastro et al. 2002; Bregman & Lloyd-Davies 2007; Yao et al. 2008).

Anderson & Bregman (2010, hereafter AB10) list a number of known indirect pieces of evidence for the Galactic corona. They attempt to use them to give limits on the amount of gas it can contain. For an isothermal corona, they argued that the gas mass should be relatively small – of the order of 10% of the total mass of missing baryons – assuming a Navarro et al. (1997) (NFW) profile. The fraction can become significantly larger, however, for *adiabatic* coronae (see also Binney et al. 2009; Fang et al. 2013). The same authors presented also a possible detection of a corona of missing baryons around the massive spiral NGC 1961 (Anderson & Bregman 2011). Their estimate of the total mass for an isothermal corona is again ~ 10 % of the baryons that should be associated with the potential well of this galaxy. This estimate comes from an extrapolation as the visible corona extends only to about $\sim 50\,\mathrm{kpc}$ from the centre. Potential problems with this detection come from the fact that this galaxy may be the result of a recent collision (Combes et al. 2009) and shows a rather disturbed H I disc that extends to a distance of 50 kpc from the centre (Haan et al. 2008). A new and more compelling detection is that of the super-massive disc galaxy UGC 12591, where the amount of gas in the corona is estimated to be between 10% (isothermal) and 35 % (adiabatic; Dai et al. 2012).

Following Shull et al. (2012), the low-redshift baryon content can be divided as follows: 1.7% in cold gas (HI and HeI), 4% in the ICM (Intra-Cluster Medium), 5% in the CGM (Circum-Galactic Medium)[1], 7% in galaxies (stars and ISM), 30% in the intergalactic WHIM (Warm-Hot Ionised Medium) and 30% in the Lyα forest. This leaves $29\pm13\%$ of the baryons still missing. From their high-resolution cosmological simulations, these authors found that about half of these missing baryons may be in a hot ($T > 10^6$ K) intergalactic WHIM phase.

In this paper, we derive the density of the corona of the Mw at large distances ($\sim 50-90\,\mathrm{kpc}$) from the centre using the population of surrounding dwarf spheroidal (dSph) satellites as a probe of the hot halo gas. dSphs are gas-free dwarf galaxies – at least down to current detection limits (e.g. Mateo 1998). They are typically located close to their host galaxy in contrast to the gas-rich dwarf irregulars (dIrrs) that lie at larger distances (Mateo 1998; Geha et al. 2006). The proximity to our Galaxy is believed to be the reason for the removal of material from the dSphs, as several other physical properties are very similar between the two types (e.g. Kormendy 1985; Tolstoy et al. 2009). A similar *distance-morphology relation* is also observed in dwarf galaxies in other groups (e.g. Geha et al. 2006), suggesting that in addition to supernova (SN) feedback, environmental effects like ram-pressure stripping from a hot corona (Gunn & Gott 1972; Nulsen 1982) or tidal stripping (e.g. Read et al. 2006b,a) must play a crucial role. There is a vast literature investigating these phenomena via hydrodynamical simulations in different environments, from galaxy clusters to MW-sized haloes (e.g. Mori & Burkert 2000; Marcolini et al. 2003; Roediger & Hensler 2005; Nichols & Bland-Hawthorn 2011),

[1] Due to the poor knowledge of such a phase, this fraction has been assumed rather than measured.

as well as observations of possible on-going ram-pressure stripping from dwarf galaxies (McConnachie et al. 2007) and normal galaxies (Fossati et al. 2012). For a study that combines ram-pressure and tidal stripping in dwarfs see Mayer et al. (2006).

Here, we concentrate on ram-pressure stripping and assume it to be the dominant mechanism that removed gas from the dSphs (tidal stripping plays a more minor role for the galaxies we study here; see §2.3 and Blitz & Robishaw 2000). We introduce a simple model of SN feedback and investigate its influence on the stripping rate. We then estimate the minimum density that the corona of the MW should have for this stripping to occur. This technique has been pioneered by Lin & Faber (1983); Moore & Davis (1994) and subsequently refined by Grcevich & Putman (2009, and see also Blitz & Robishaw 2000), who considered a simple analytical formula for the stripping, applied it to four dSphs, and found that the number density of the hot halo within $\sim 120\,\mathrm{kpc}$ from the centre of the MW is of the order of a few times $10^{-4}\,\mathrm{cm}^{-3}$. In this paper, we improve on these earlier works by adding several novel features:

(i) we perform hundreds of 2D hydrodynamical simulations of gas stripping;

(ii) we use the measured star formation histories (SFHs) for the dwarfs to derive the time at which they last lost their gas and, using a modified version of the Kennicutt-Schmidt (K-S) relation (Schmidt 1959; Kennicutt 1998b), we determine their internal gas density at that time;

(iii) we use a detailed reconstruction of the orbits of the dwarfs that fully marginalizes over uncertainties in their distances, line-of-sight velocities and proper motions;

(iv) we include a model for SN feedback with discrete energy injections to assess the importance of internal versus external gas loss mechanisms; and

(v) we use pressure confinement arguments (similar to Spitzer (1956) but applied to the dSphs) to derive an *upper bound* on the coronal density.

We use the Sextans and Carina dwarfs, which are suitable for this study because they are small systems with reliable SFHs and mass estimates. Moreover they have similar pericentric radii but totally different SFHs, providing an excellent consistency test of our method.

This paper is organized as follows. In §2, we estimate the effect of ram-pressure stripping on dwarf galaxies. We estimate the relative importance of tidal stripping for the two dSphs we study here, and we introduce the key concepts used in this paper to derive our lower and upper bounds on the coronal gas density. In §3, we describe our numerical method and initial conditions. In §4, we show our results. In §5, we wrap in other constraints on the coronal density from the literature and discuss the implications of our results for the missing baryon problem. Finally, in §6 we present our conclusions.

2 ANALYTIC RESULTS

2.1 Ram-pressure stripping: a lower bound on the hot corona density

To leading order, a dwarf galaxy will be ram-pressure stripped of its ISM if (Gunn & Gott 1972):

$$\rho_{\rm cor} v^2 \gtrsim \rho_{\rm gas}\sigma^2 \ , \qquad (1)$$

where $\rho_{\rm cor}$ is the density of the background medium (the Galactic corona) that we would like to measure, v is the velocity of the dwarf galaxy, $\rho_{\rm gas}$ is the density of gas in the dwarf's ISM and σ is the velocity dispersion of the dwarf (a proxy for its mass).

The velocity of the dwarf v is maximized at the pericentre of the orbit, as is the background density $\rho_{\rm cor}$. Thus, we can reasonably expect almost all of the ram-pressure stripping to occur at or near to a pericentric passage. At the orbital pericentre $r_{\rm p}$, equation (1) can be recast as:

$$\rho_{\rm cor}(r_{\rm p})|_{\rm min} = \frac{\rho_{\rm gas}\sigma^2}{v(r_{\rm p})^2} \ , \qquad (2)$$

which gives the minimum coronal density at $r_{\rm p}$ required to strip the dwarf of all of its ISM, assuming that $\rho_{\rm gas}$ is the density of the latter just before the stripping event.

The velocity of the dwarf at the pericentre $v(r_{\rm p})$ and the pericentre value $r_{\rm p}$ are easily determined once the orbit is known. Dwarf orbits can be reconstructed by assuming simple spherical potential models for the MW up to ~ 2 orbital periods backwards in time (Lux et al. 2010), and in some cases even more depending on how close to spherical the background potential is, and whether or not the dwarf fell in isolation or inside a 'loose group'. The velocity dispersion of the dwarf σ can be obtained from stellar kinematic measurements (e.g. Walker et al. 2009), which just leaves the ISM density $\rho_{\rm gas}$ as a free parameter. A novel key aspect of this work is that we introduce a new method for estimating $\rho_{\rm gas}$. Using deep resolved colour magnitude diagrams, and fitting stellar population synthesis models, the SFH of the nearby MW dwarf galaxies can be inferred (e.g. Dolphin et al. 2005). This gives us the star formation rate as a function of time from which we can derive the last moment at which the dwarf had gas available to form fresh stars. Furthermore, through a modified version of the K-S relation, we can estimate the gas surface density at this time, $\Sigma_{\rm gas}$ (see §3.3). Assuming spherical symmetry and de-projecting we get the ISM density $\rho_{\rm gas}$. All this information can then be used to solve equation (2) for $\rho_{\rm cor}(r_{\rm p})|_{\rm min}$.

In practice, we actually simulate the passage of a dwarf through pericentre in order to retrieve more accurate results with respect to the analytic ones. The simulations also allow us to include the effect of stellar feedback. Equation (2), however, remains useful as it captures the essence of our methodology. We consider the accuracy of using equation (2) as opposed to the full hydrodynamic simulations in §5.2.

2.2 Pressure confinement of the dwarf ISM: an upper bound on the hot corona density

A novel idea in this work is to use the pressure confinement of the dwarf ISM to obtain an *upper bound* on the hot corona density (c.f. Spitzer 1956). Matching the internal pressure of

dSph	Distance (kpc)	L_V ($10^6 L_\odot$)	r_p (kpc)	r_a (kpc)	t_orb (Gyrs)	r_last (kpc)	$M_\mathrm{DM}(r_\mathrm{last})$ ($10^7\,\mathrm{M}_\odot$)	t_lb (Gyrs)
Sextans	86 ± 4	0.5	60 ± 20	200 ± 100	4 ± 3	1	2	~ 7
Carina	101 ± 5	0.43	50 ± 30	110 ± 30	1.8 ± 0.8	0.87	3.7	~ 0.5

Table 1. Physical properties of the Carina and Sextans dSph galaxies. From left to right, the columns show the distance to the dwarf, the V-band luminosity, the pericentre and apocentre, the orbital period, the radius to the last measured kinematic data point r_last, the mass within r_last, and the time to the last star formation burst t_lb. Data are taken from Mateo (1998) (distance, L_V), Walker et al. (2009) (r_last, $M_\mathrm{DM}(r_\mathrm{last})$), Lux et al. (2010) ($r_\mathrm{p}$, r_a, t_orb). t_lb has been derived from the SFHs in Lee et al. (2009) (Sextans) and Rizzi et al. (2003) (Carina).

the dwarf ISM with the external pressure from the hot halo, we have:

$$\rho_\mathrm{gas} T_\mathrm{gas} \sim \rho_\mathrm{cor} T_\mathrm{cor} \ , \tag{3}$$

where $T_\mathrm{gas} \sim 10^4\,\mathrm{K}$ is the temperature of the dwarf galaxy ISM, and $T_\mathrm{cor} \sim 10^6\,\mathrm{K}$ is the temperature of the MW hot corona. Thus, for a given total gas mass in the dwarf M_gas, the dwarf ISM gas will extend to some maximum radius:

$$r_\mathrm{gas} \sim \left[\frac{3 M_\mathrm{gas}}{4\pi\rho_\mathrm{cor}} \frac{T_\mathrm{gas}}{T_\mathrm{cor}} \right]^{1/3} \ . \tag{4}$$

We know M_gas from the SFH (see §2.1) while T_gas and T_cor follow from our potential models for the dwarf and the MW. Thus, we can estimate ρ_cor simply from r_gas. If we allow r_gas to extend to infinity, then we obtain essentially no bound on ρ_cor. However, if we assume some minimum $r_\mathrm{gas}|_\mathrm{min}$, then we obtain an upper bound on the hot corona density $\rho_\mathrm{cor}|_\mathrm{max}$.

We assume here that $r_\mathrm{gas}|_\mathrm{min}$ is set by the radius within which the SFH history is derived (r_SF, see later). This assumption is sensible since at the time of the last star formation event, the gas had to be at least as extended as the stars that formed from it. It is also self-consistent since r_SF is the radius out to which we estimate M_gas. However, it relies on the stellar distribution not significantly expanding after its stars formed. Tidal shocking (e.g. Read et al. 2006b) and/or collisionless heating due to SN feedback (e.g. Read & Gilmore 2005; Teyssier et al. 2013) could both cause the stellar distribution to expand. For Sextans, which had its last burst long ago, this could be a potential worry; for Carina, which had its last burst very recently, the effect should be small (see Fig. 2). In §5, we show that additional constraints from pulsar dispersion and X-ray emission measurements give an independent upper bound that is consistent or stronger than that derived from pressure confinement. This suggests that our assumption that $r_\mathrm{gas}|_\mathrm{min} \sim r_\mathrm{SF}$ is sound.

In practice, we must solve equation (4) *iteratively* since we do not know ρ_cor, yet we require r_gas to calculate ρ_cor. We describe this iterative calculation in §3.3 where a more realistic gas distribution, derived from the reconstruction of the SFH of the dwarf galaxy, is also used.

2.3 Tidal stripping and shocking

In addition to ram-pressure stripping, dwarf galaxies will also experience tidal stripping and shocking. Tidal stripping becomes important roughly when the dynamical density of the dwarf matches the dynamical density of the host galaxy. As for ram-pressure stripping, this is most effective at pericentre (e.g. Read et al. 2006b):

$$r_\mathrm{t} \sim \left[\frac{M_\mathrm{d}}{3 M_\mathrm{h}} \right]^{1/3} r_\mathrm{p} \ , \tag{5}$$

where M_h and M_d are the dynamical masses of the host galaxy and the dwarf, respectively, and r_t is the tidal stripping radius outside of which tidal stripping will become important. For typical MW dwarf galaxies like those we consider here, $r_\mathrm{p} \gtrsim 30\,\mathrm{kpc}$ (e.g. Lux et al. 2010), $M_\mathrm{d} \gtrsim 3 \times 10^7\,\mathrm{M}_\odot$ (e.g. Walker et al. 2009, and see Table 1), and $M_\mathrm{h}(< r_\mathrm{p}) \sim 2 \times 10^{11}\,\mathrm{M}_\odot$ (e.g. Klypin et al. 2002). This gives $r_\mathrm{t} \gtrsim 1.1$ kpc, which agrees well with the more careful analysis presented in Read et al. (2006a).

Whether significant gas will be tidally stripped from the dwarf then depends on whether the dwarf ISM extends beyond the tidal stripping radius. Using equation (4) and assuming a typical gas mass of $M_\mathrm{gas} \sim 10^6\,\mathrm{M}_\odot$; a coronal density of $n_\mathrm{cor} \sim 2 \times 10^{-4}\,\mathrm{cm}^{-3}$; and $T_\mathrm{gas}/T_\mathrm{cor} \sim 0.01$ gives $r_\mathrm{gas} \sim 0.9\,\mathrm{kpc}$. Thus, $r_\mathrm{gas} < r_\mathrm{t}$ and we do not expect the gas in the dwarf to experience significant tidal stripping (see also a similar calculation in Blitz & Robishaw 2000). Read et al. (2006a) also estimate the likely effect of tidal shocking, finding that it is unimportant unless $r_p \lesssim 20\,\mathrm{kpc}$ which is unlikely for the dwarfs we study here (Lux et al. 2010).

For the above reasons, we model only the ram pressure stripping of the dSphs in this work, deferring tides and/or other collisionless heating effects to future work.

2.4 Adiabatic versus isothermal coronae

While it is likely that the MW has a hot corona of gas, it remains unclear what its thermodynamic state should be. Recent cosmological simulations produce a hot corona that is neither isothermal nor adiabatic (Crain et al. 2010), although these simulations are presently unable to make fully ab-initio predictions for disc galaxies in the real Universe (e.g. Mayer et al. 2008). For this reason, we consider here three cases of a fully isothermal, a fully adiabatic and an intermediate-state (so-called 'cooling') corona. Assuming a polytropic equation of state $P = A\rho^\gamma$ for the gas, spherical symmetry, a background potential model for the MW $\Phi(r)$, and hydrostatic equilibrium, we may calculate the expected gas density profile ρ by balancing pressure forces and gravity ($\nabla p = -\rho \nabla \Phi$; e.g. Binney et al. 2009) which gives:

$$\rho = \begin{cases} \rho_0 \left[1 - (\Phi - \Phi_0) \frac{\gamma - 1}{\gamma A} \right]^{\frac{1}{\gamma - 1}} & \gamma \neq 1 \\ \rho_0 \exp\left(-\frac{\Phi - \Phi_0}{A} \right) & \gamma = 1 \end{cases} \ , \tag{6}$$

where ρ_0 and Φ_0 are, respectively, the density and potential at the reference radius r_0. For isothermal haloes, $\gamma = 1$

and we may write $P = A\rho \propto \rho T$ and therefore $T = T_0 =$ const., as expected. For adiabatic haloes, $\gamma = 5/3$. Thus, we consider models in the range $1 \leqslant \gamma \leqslant 5/3$. Note that the potential $\Phi(r)$, ρ_0, γ and A are all effectively free parameters in this model which must be matched to the MW.

Throughout the paper, we will assume a truncated flat (TF) potential model for the MW (Wilkinson & Evans 1999):

$$\Phi(r) = -\frac{GM}{a}\ln\Big(\frac{\sqrt{r^2+a^2}+a}{r}\Big)\ , \qquad (7)$$

with $a = 170$ kpc and $M = 1.9 \cdot 10^{12}$ $\mathrm{M}_\odot$. This was one of two profiles used by Lux et al. (2010) to determine the orbits the MW dwarfs, and for consistency we use the same potential in all our calculations. Lux et al. (2010) found that within current observational uncertainties, the choice of potential does not significantly affect the orbit determination. In fact, for highly eccentric orbits, only the potential at pericentre $\Phi(r_\mathrm{p})$ is relevant for the purpose of this work[2]; at $30 \lesssim r_\mathrm{p} \lesssim 100$ kpc this is reasonably well constrained for the MW (e.g. Binney & Tremaine 2008).

If we probe only one – or several very similar – r_p across several dwarfs, then equation (6) is only required to *extrapolate* our results to larger and smaller radii. We must assume some value for the coronal temperature $T_\mathrm{cor}(r_\mathrm{p})$. But we may then after-the-fact assume an adiabatic or isothermal corona and explore what this means e.g. for the missing baryon fraction in the MW (see §5.1). If, however, we have data at multiple r_p of wide separation then we must specify a model up-front since the temperature T_cor (required to calculate r_gas; see equation (4)) is in general a function of radius through equation (6): we must perform a joint analysis of all dwarfs simultaneously. For the moment, we restrict our analysis to two dwarfs (Sextans and Carina) with very similar r_p within their uncertainties (see Table 1). We model each dwarf separately using this independent analysis as a consistency check of our methodology and its assumptions. In the future, it would be interesting to analyse the only dwarf (Fornax) with pericentre radius significantly different from Carina and Sextans ($r_\mathrm{p} = 110 \pm 20$ kpc). However, Fornax is 30 times more luminous than our two dwarfs and to obtain reliable results from the simulations will be much more challenging since it would require about 10^2 times more grid points than our current simulations (and possibly 3D simulations).

[2] To see why that is the case, notice that in the limit $r_\mathrm{a} \gg r_\mathrm{p}$, and assuming spherical symmetry, the pericentre of the dwarf orbit is completely determined by its specific angular momentum (e.g. Read et al. 2006b):

$$J^2 \simeq -2r_\mathrm{p}^2\Phi(r_\mathrm{p})\ , \qquad (8)$$

while the velocity at pericentre is then simply $v_\mathrm{p} = J/r_\mathrm{p}$. The dwarf's specific angular momentum J simply follows from its current distance from the centre of the MW and its tangential velocity $J = dv_\mathrm{t}$ that comes from a mixture of its doppler velocity and proper motion (depending on its orientation on the sky). Thus, for eccentric orbits, r_p follows observationally from a measurement of J, and a model assumption about $\Phi(r_\mathrm{p})$.

3 METHOD

We use the code ECHO++ (Marinacci et al. 2010, 2011), an Eulerian fixed-grid code based on Del Zanna et al. (2007), to run a series of high-resolution, two-dimensional hydrodynamical simulations of dwarf galaxies moving through a hot rarefied medium, representative of the Galactic corona. The simulations were performed over a Cartesian grid with open boundaries. The dwarf galaxy is located on the $y = 0$ axis and embedded in a hot medium, which moves along the x-axis with a speed that varies with time, allowing us to model the motion of the dwarf along its orbit. The simulations include both radiative cooling and SN feedback. In the following subsections we describe the initial conditions.

3.1 DM and coronal gas

We set up a dwarf galaxy as a spherical distribution of cold isothermal gas ($T_\mathrm{gas} = 1 \times 10^4$ K) in hydrostatic equilibrium in a fixed potential. Given that dSphs have mass-to-light ratios typically above 10 (e.g., Battaglia et al. 2008), we assume that the potential is totally dominated by DM, and we neglect both the stellar mass and the self gravity of the gas. The gravitational force, which determines the initial cold gas distribution profile and at the same time counteracts the ram pressure, is computed by using the NFW profiles taken from Walker et al. (2009) (see Table 1). For each dwarf, the spherical DM halo is located at the centre of the computational box. Note that the DM parameters used in this work refer to present-day observations. Since tidal stripping can remove DM from these haloes, we are potentially underestimating the gravitational restoring force which acted against the ram-pressure at the time of the last stripping event. As a consequence the coronal value recovered with Sextans might in principle be higher than the value obtained, while Carina should not be affected given that the last stripping event occurred very recently.

The cold medium of the dwarf is in pressure equilibrium with an external hot medium, which represents the Galactic corona. This hot medium fills the whole computational box and it is assumed to have constant density, temperature and metallicity; it moves along the x-axis with a velocity that depends on the orbital path of the dwarf (see §3.2). The metallicity of the corona is fixed to 0.1 $Z_\odot$ in agreement with the recent observational determinations for NGC 891 (Hodges-Kluck & Bregman 2013), while our default corona temperature is $T_\mathrm{cor} = 1.8 \times 10^6$ K (Fukugita & Peebles 2006). Different temperatures for the coronal gas are investigated in §4.4.

The last parameter to set is the number density of the coronal gas n_cor, which is the goal of our investigation. In the following, with n_cor we refer to the total number density, which for a completely ionized medium is the sum of the number density of ions n_i and of electrons n_e. We assume an abundance of helium of 26.4% from big bang nucleosynthesis considerations, which makes the electron density $n_\mathrm{e} \simeq 1.1\, n_\mathrm{i}$. The coronal density is then found iteratively, by running several simulations and finding the value that produces the complete stripping of cold gas from the dwarf at the end of the run. Note that n_cor also sets the pressure of the external medium, which in turn determines the radius at which the

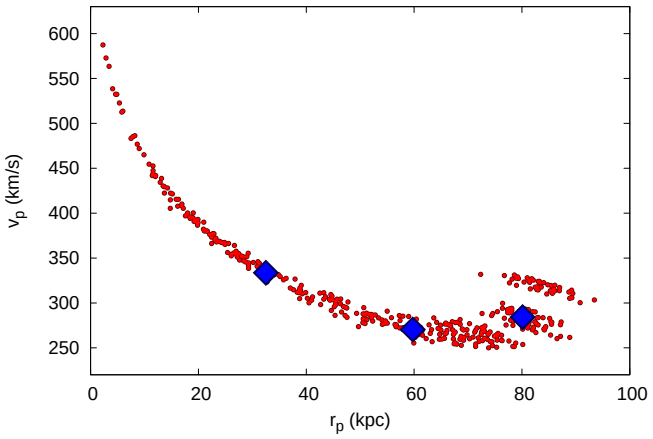

Figure 1. Pericentric radii and velocities for the orbits of the Sextans dSph compatible with a pericentric passage at the stripping time ($t_{\rm lb}$) determined from the SFH (see the text). The large (blue) diamonds show the three representative orbits (median, first and third quartiles in $r_{\rm p}$ and in $v_{\rm p}$ within ± 3 kpc from the selected value of $r_{\rm p}$) chosen for our simulations.

pressure equilibrium is reached. We return to this point in §3.3.

3.2 Orbits

One of the basic parameters that have to be set in our simulations is the relative velocity between the dwarf and the surrounding medium, which requires the knowledge of the orbital path of the satellite galaxy in the potential of the MW. For this purpose, we use the reconstruction of the dwarf orbits derived by Lux et al. (2010). These authors provide a set of 1000 possible orbits for each dwarf given the potential of the MW and the, unfortunately poorly constrained, proper motions of the dwarfs. They considered two Galactic potentials: the TF model (Wilkinson & Evans 1999, and equation 7) and the Law et al. (2005) model. In this work we only use the former. As discussed in §2.4, we are not very sensitive to the choice of potential models: uncertainties in the orbit coming from proper motion errors and other model systematics will dominate our error budget. When *extrapolating* our results to larger radii, however, the choice of the potential model and the assumed thermodynamic state of the hot coronal gas become important. We discuss this further in §5.1.

The families of orbits for each dSph are classified in terms of the pericentric radius ($r_{\rm p}$) and the velocity at pericentre ($v_{\rm p}$). We select only the orbits having pericentric passages compatible with our estimate of look-back time of the last burst of star formation $t_{\rm lb}$ (see §3.3). In practice, given $t_{\rm lb}$ and the width of the last SFR temporal bin, we accept only the orbits which have a pericentric passage within this bin. Fig. 1 shows the distribution of these orbits in the ($r_{\rm p}$, $v_{\rm p}$) space. Given the non-triviality of this distribution we decide to focus on three representative orbits. The median orbit is given by the median value of the pericentric radius $\bar{r}_{\rm p}$ and the median of $\bar{v}_{\rm p}$ in the range ± 3 kpc around $\bar{r}_{\rm p}$. For Sextans, we obtain $\bar{r}_{\rm p} = 59.8$ kpc and $\bar{v}_{\rm p} = 270.4\,{\rm km\,s^{-1}}$, in agreement with the values obtained by Lux et al. (2010) for the last pericentric passage. We then select two more orbits at the first and third quartiles of the distribution of $r_{\rm p}$ and their corresponding values of $v_{\rm p}$. The selected orbits are indicated by the large diamonds in Fig. 1.

Thus, as far as the orbits are concerned, we perform three distinct sets of hydrodynamical simulations. The parameters of the three representative orbits for Sextans are reported in Table 5. We show in §4.2 that the results for Sextans' orbits are remarkably consistent with each other despite the large difference in their input parameters. This is an encouraging test of our model assumptions and systematics. Given these results, we consider only the median orbit for Carina.

The typical orbital periods of our two dwarfs are between 1 and 4 Gyr. However, the stripping process is much more efficient at and near the orbital pericentre and we can save computational time by simulating only that part of the orbit. To have an idea of the variation of the stripping efficiency within an orbit one can make use of equation (1) to obtain:

$$\varepsilon_{\rm strip}(r) = \frac{v(r)^2}{v_{\rm p}^2}\,\frac{n_{\rm cor}(r)}{n_{\rm cor,p}}\ , \qquad (9)$$

where $v(r)$ and $r(t)$ are the position and velocity of the dwarf along its orbit at time t; $n_{\rm cor}(r)$ is the coronal density at r; and $n_{\rm cor,p}$ is the coronal density at pericentre. For our two dwarfs, the efficiency calculated from equation (9) changes by a factor of $\sim$10 from pericentre to apocentre. After performing a series of simulations progressively enlarging the computational time up to the full length of the orbit we find that including in the calculation regions where the efficiency has dropped below 50% from the pericentre does not result in any appreciable difference in the derived coronal density. Thus, we focus on the part of the orbit with efficiency above 50%, which leads to the integration times reported in Tables 4 and 5. The x-component of the velocity of the hot gas is set according to the relative velocity $v(r(t))$, which in turn depends on the selected orbit. For simplicity, we keep the value of the coronal density constant in our simulation. In this way we derive an *average* value of the coronal density over the orbit segment around the pericentre. Finally, we vary $n_{\rm cor}$ until we find the value that produces a complete removal of gas from the dwarf galaxy: $n_{\rm cor}|_{\rm min}$.

3.3 Initial gas distribution

In our simulations, the ISM of the dwarf galaxies is composed by isothermal ($T = 10^4\,{\rm K}$) gas that is in hydrostatic equilibrium with the DM potential and has a subsolar metallicity taken from the literature (see Table 4). Note that the metallicity of the coronal gas is always set to $0.1\,Z_\odot$ (see §3.1). The radius at which the cold gas distribution is truncated corresponds to the radius where its pressure is equal to the pressure of the coronal gas. The latter depends on the coronal temperature, for which we explore different values, $T_{\rm cor} = 1,\ 1.8,\ 3\times10^6\,{\rm K}$ (see again §3.1 and 4.4). Since the gravitational potential of the DM halo is fixed, the gas density distribution in the dwarf is fully determined once we set the central density. We estimate this central density using information contained in the SFH, as described below.

We derived the look-back time of the last burst of star formation ($t_{\rm lb}$) as the time when the estimated value of the

dSph	$r_{\rm SF}$ (kpc)	$t_{\rm lb}$ (Gyr)	SFR ($\rm M_\odot yr^{-1}$)	$\Sigma_{\rm SFR}$ ($\rm M_\odot yr^{-1} kpc^{-2}$)	$\bar{n}_{\rm gas}$ ($\rm cm^{-3}$)	$n_{0,\rm gas}$ ($\rm cm^{-3}$)	$r_{\rm gas}$ (kpc)	$M_{\rm gas}$ ($\rm M_\odot$)
Sextans	0.5	7	$4.6 \pm 2.2 \times 10^{-5}$	5.9×10^{-5}	0.09	0.27	0.98	7×10^6
Carina	0.28	0.5	$4.6 \pm 1.3 \times 10^{-6}$	1.9×10^{-5}	0.14	0.4	0.4	6.3×10^5

Table 2. Star formation properties and derived cold gas content of our two dSphs at the time of the last ram-pressure stripping event. The SFRs and gas density distributions are used as initial conditions for our hydrodynamical simulations. From left to right, the columns show the radius at which the SFR has been extrapolated; time to the last star formation burst; star formation rate at $t_{\rm lb}$; SFR surface density at $t_{\rm lb}$ $\Sigma_{\rm SFR} = {\rm SFR}/(\pi r_{\rm SF}^2)$; initial mean cold gas density; initial central gas density; computed radius of the cold gas distribution; computed initial cold gas mass within $r_{\rm gas}$.

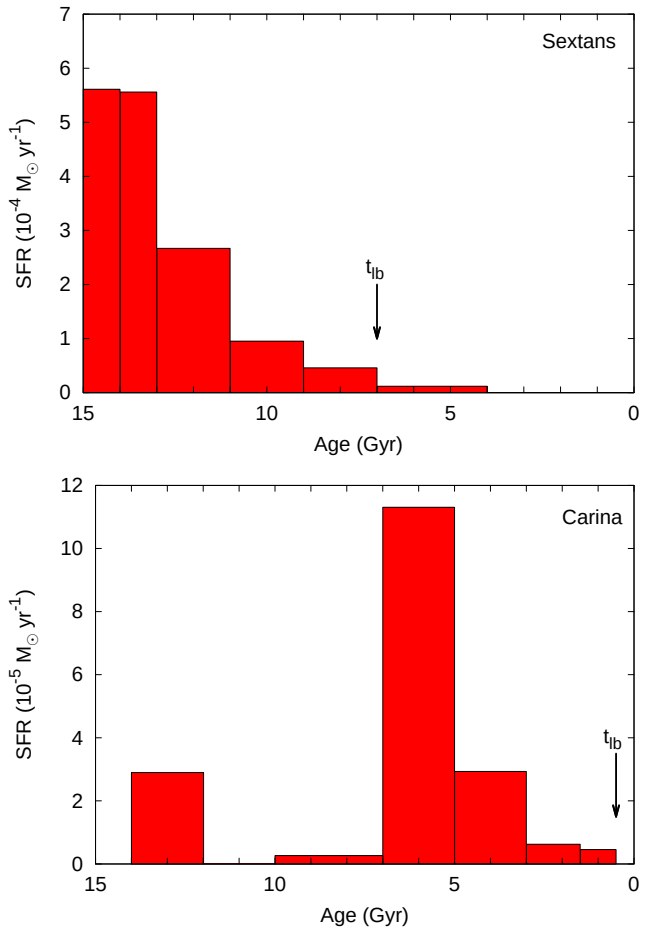

Figure 2. SFH of Sextans from Lee et al. (2009) and of Carina from Rizzi et al. (2003). The arrow indicates the look-back time of last burst of star formation. In our scheme, this corresponds to the last stripping event.

SFR is consistent with zero within the given uncertainties. At that time, we assume that the dwarf has a negligible amount of gas left, i.e. we consider the gas stripping process as completed. In Table 1, we report the times of the last stripping event for the dSphs. We refer to this as the *last* stripping event because it is likely that dSphs have suffered gas stripping also at earlier times. Considering only the last event has a number of advantages: (i) it saves computational time; (ii) it allows us to probe the corona at the closest possible look-back time; and (iii) most importantly, it allows for the best possible reconstruction of the orbital paths (see §3.2).

The SFHs of Sextans and Carina, taken from Lee et al. (2009); Rizzi et al. (2003), are shown in Fig. 2. The look-back times of the last starburst (i.e., the last stripping event) are $t_{\rm lb} \sim 7$ and 0.5 Gyr, respectively. From the SFHs we can then extract the SFRs at the time prior to this event. These values are reported in Table 2.

There are two key uncertainties related to our reconstruction of the SFR at a given look-back time:

(i) The time resolution of the SFH makes the $t_{\rm lb}$ uncertain by about $0.5-1$ Gyr. This is a small error compared to other uncertainties.

(ii) The presence of 'blue straggler stars' may contaminate the SFH, masquerading as recent star formation. Lee et al. (2009) explicitly consider this, publishing an alternate 'corrected' SFH for Sextans. The corrected SFH has no star formation at $t > t_{\rm lb}$, and a small reduction in star formation at $t_{\rm lb}$. We preferred to use the uncorrected SFH shown in Fig. 2 because it is consistent with the one used for Carina (where the correction has not been applied). However, we explicitly tested for the effect of blue straggler contamination on our results by running some additional simulations using the corrected SFH of Lee et al. (2009). We found that the final value of the coronal density does not vary appreciably within our quoted uncertainties.

Once we know the SFR before stripping, we use a revised version of the K-S relation to estimate the gas density at that time. The standard K-S relation connects the (molecular and atomic) hydrogen surface density, $\Sigma_{\rm H\,I}$ and $\Sigma_{\rm H_2}$, and the SFR surface density, $\Sigma_{\rm SFR}$, with a power-law (slope 1.4). It is valid for disc galaxies and starburst galaxies (e.g, Kennicutt 1998a). It is well known that this relation steepens considerably for column densities below $\sim 10\,\rm M_\odot pc^{-2}$ (e.g. Leroy et al. 2008). While the $\Sigma_{\rm SFR}$ seems to correlate very well with the molecular gas surface density (Bigiel et al. 2011), the relation breaks down at low densities likely due to the transition from a molecular-dominated to an atomic-dominated ISM (Krumholz et al. 2012). Due to the low values of the SFRs of our dwarfs (see Table 2), the expected $\Sigma_{\rm H\,I+H_2}$ falls below the limit and the dwarfs' ISM is dominated by H I, as confirmed by observations (see Table 3 and references therein). In this paper, we do not distinguish between different gas phases in the ISM as in the simulations the cooling is truncated at 10^4 K. This is an acceptable approximation since our star formation and feedback prescriptions are purely empirical and based on the observed SFR.

To date, there is no consensus on how to extend the K-

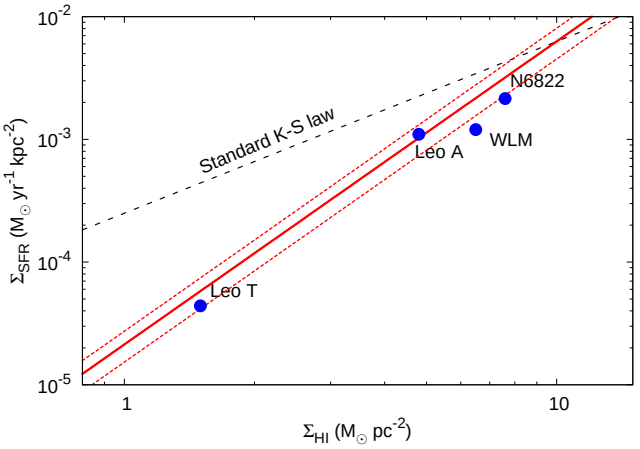

Figure 3. K-S relation for dwarf galaxies as described by equation (10). The points show the location of four Local Group dIrrs (see Table 3).

Galaxy	Σ_{SFR} ($M_\odot$yr^{-1}kpc^{-2})	Σ_{HI} ($M_\odot$pc^{-2})	Σ_{H_2} ($M_\odot$pc^{-2})	Ref.
NGC 6822	2.15×10^{-3}	7.6	1.1	(1,2,3)
WLM	1.2×10^{-3}	6.5	Negligible	(4,5,6)
Leo A	1.1×10^{-3}	4.8	Missing	(7,8)
Leo T	4.4×10^{-5}	1.5	Missing	(9,10)

Table 3. SFR densities and gas densities for four dIrrs of the Local Group. CO is not detected in Wolf-Lundmark-Melotte (WLM), and there is only an upper limit, while for Leo A and Leo T such studies are missing in the literature. References to the SFR, H I and CO studies (when applicable): (1) Efremova et al. (2011), (2) de Blok & Walter (2006), (3) Israel (1997), (4) Dolphin (2000), (5) Kepley et al. (2007), (6) Taylor & Klein (2001), (7) Cole et al. (2007), (8) Young & Lo (1996), (9) de Jong et al. (2008), (10) Ryan-Weber et al. (2008).

S relation to surface densities $< 10\,M_\odot pc^{-2}$. Some authors have however studied the location of dwarf galaxies in the (Σ_{SFR}, Σ_{HI}) plane. Bigiel et al. (2010) studied five dwarf galaxies and found a relation $\Sigma_{SFR} \propto \Sigma_{HI}^{1.7}$. Using a larger sample of 23 very faint dwarf galaxies, Roychowdhury et al. (2009) found that these systems depart systematically from the standard K-S relation but they, quite remarkably, follow the Kennicutt relation for disc galaxies only (excluding starburst galaxies; Kennicutt 1998b). This relation can be written as follows:

$$\Sigma_{SFR} = (2.13 \pm 0.6) \cdot 10^{-5}\ \Sigma_{gas}^{2.47}\ . \qquad (10)$$

Note that Σ_{SFR} is given in $M_\odot yr^{-1}kpc^{-2}$ and Σ_{gas} in $M_\odot pc^{-2}$. In the following we adopt equation (10), where the normalization factor and the associated errors (roughly 1σ) have been taken from the standard K-S relation using the normalization of Roychowdhury et al. (2009).

To make sure that equation (10) is suitable for our purposes, we check that it holds for galaxies in the Local Group. We consider four dIrrs that span a large range of gas and SFR surface densities. For each of them, we calculate Σ_{SFR} knowing the value of the SFR and the area of the galaxy from which it has been derived. We then estimate the surface densities of H I and molecular gas (when present) averaged over the same area. The obtained values are listed in Table 3. As expected, the molecular phase plays a minor role and can safely be neglected. In Fig. 3 we show the obtained values of Σ_{SFR} and Σ_{HI} (solid circles), as well as the relation from equation (10). The agreement is remarkably good for all the dIrrs, the dashed lines show the 1σ error. Note that the standard K-S relation (dashed line) would clearly overestimate Σ_{SFR} at these gas surface densities by up to an order of magnitude.

Using Σ_{SFR} reported in Table 2, we estimate the average gas volumetric density (assuming spherical symmetry) for the two dSphs by inverting equation (10):

$$\overline{\rho}_{gas}(< r_{SF}) = \frac{3}{4 r_{SF}} \left(\frac{\Sigma_{SFR}(< r_{SF})}{2.13 \times 10^{-5}} \right)^{\frac{1}{2.47}}\ , \qquad (11)$$

where r_{SF} is the radius within which the SFH has been derived[3]. The gas density profile is then rescaled to match this average density within r_{SF}. This allows us to determine the central density $n_{0,gas}$ and the total gaseous mass of the dwarf within r_{gas}, which is the radius at which pressure equilibrium with the corona is reached. The densities are then multiplied by a factor 1.36 to take into account the He fraction. All these parameters are reported in Table 2.

3.4 Radiative cooling, star formation and feedback

Radiative cooling is included in the code by taking the collisional ionization equilibrium cooling function of Sutherland & Dopita (1993). The cooling term is added explicitly to the energy equation of the gas and, for stability reasons, the hydrodynamic time-step is reduced to 10% of the minimum cooling time in the computational domain. Metal cooling is taken into account and the metallicity of the gas is treated as a passive scalar field advected by the flow. The cooling rate is set to zero below $T_{min} = 10^4$ K.

We include star formation in our hydrodynamical code by introducing a temperature cut, $T_{cut} = 4 \times 10^4$ K. Only cells below this temperature are allowed to form stars. The amount of gas converted into stars is computed from equation (10), where the gas density is a function of time. However, given that the star formation rates used for our simulated dwarfs are small (see Table 2), there is no significant depletion of gas. This is an important point as it shows that the removal of gas from Sextans and Carina can not be achieved by star formation alone. Rather, it requires additional processes, i.e. a combination of SN feedback and gas stripping.

Concerning SN explosions, we assume that our SN bubbles start their expansion at the end of the adiabatic (Sedov) phase and we only follow the subsequent radiative phase. In this phase, the thermal energy is lost due to radiative cooling and adiabatic expansion, while the kinetic energy is used partially for the expansion and partially it is transferred to

[3] It is worth mentioning that equation (11) derives from a slightly different definition of Σ_{gas}. This is due to the fact that our dwarfs have to be considered spheroidals, while equation (10) formally holds only for discs.

Run	$L_{\rm box}$ (kpc)	Δx (pc)	$T_{\rm cor}$ (K)	$n_{0,\rm gas}$ ($\rm cm^{-3}$)	Z ($Z_\odot$)	$\overline{v}_{\rm sat}$ (km/s)	Δr (kpc)	Δt (Myr)
SextansMidMed	80	34	1.8×10^6	0.27	0.02	228	59.8–90.2	930
SextansLowMed	80	39	1.8×10^6	0.18	0.02	228	59.8–90.2	930
SextansMid1stQ	60	34	1.8×10^6	0.27	0.02	286	33.9–59.2	420
SextansLow1stQ	60	39	1.8×10^6	0.18	0.02	286	33.9–59.2	420
SextansMid3rdQ	100	34	1.8×10^6	0.27	0.02	246	80.4–131.5	1220
SextansLow3rdQ	100	39	1.8×10^6	0.18	0.02	246	80.4–131.5	1220
CarinaMidMed	80	31	1.8×10^6	0.4	0.01	251	51.2–81.8	740
CarinaLowMed	80	35	1.8×10^6	0.31	0.01	251	51.2–81.8	740
CarinaMidMed1e6K	80	31	1×10^6	0.4	0.01	251	51.2–81.8	740
CarinaMidMed3e6K	80	31	3×10^6	0.4	0.01	251	51.2–81.8	740

Table 4. Parameters of the simulations. Each run is denoted by the dwarf name, the initial density of the dwarf's ISM (see §3.3 and 4.2), the pericentric distance of the orbit and the temperature of the corona (if different from the reference value $T_{\rm cor} = 1.8\times10^6$ K). $L_{\rm box}$ is the size of the computational domain in each direction, Δx is the resolution, $T_{\rm cor}$ is the coronal temperature, $n_{0,\rm gas}$ is the initial central density of the dwarf, Z is the dwarf's gas metallicity, $\overline{v}_{\rm sat}$ is the dwarf velocity averaged over the simulated distance range Δr and Δt is the integration time corresponding to the part of the orbits with stripping efficiency greater than 50%.

the ambient medium at later times. The explosion of a single SN is implemented by increasing the volumetric thermal energy density by a factor $\frac{E_{\rm SN}}{V_{\rm Sedov}}$, where $E_{\rm SN} = 10^{51}$ erg and $V_{\rm Sedov} = \frac{4}{3}\pi r^3_{\rm Sedov}$ represents the initial spherical volume of the bubble, with $r_{\rm Sedov}$ the radius of the injection region. For every different gas profile, $r_{\rm Sedov}$ – the SN bubble radius at the end of the adiabatic phase – is determined by running very-high resolution simulations of a single SN exploding in the centre of the dwarf. $r_{\rm Sedov}$ is then set to the value of the initial radius that produces a match between the simulated evolution of the SN shock radius and the analytical (two-dimensional) one for the radiative phase. We model a SN bubble at the explosion time with just four cells, since higher numbers cause our simulations to be too demanding from a numerical point of view. Thus, the resolution of a simulation is defined by the value of $r_{\rm Sedov}$ by simply equating the circular area of the SN bubble with the Cartesian one of four cells. We also adopt the overcooling correction method described in Anninos & Norman (1994).

We compute the supernova rate (SNR) from the SFR using the initial mass function (IMF) $\Psi(M)$ chosen to retrieve the SFH of our dwarf galaxies. For Sextans and Carina, a Salpeter IMF (Salpeter 1955) was assumed (see Rizzi et al. 2003; Lee et al. 2009). In this case SNR $\simeq \frac{6\times10^{-3}}{\rm M_\odot}$SFR $\frac{\rm SN}{\rm yr}$, with the SFR expressed as $\rm M_\odot\ yr^{-1}$. Applying for the SFR found in every cell with $T < T_{\rm cut}$ and multiplying the obtained SNR with the time-step, we find the number of SN "events" occurring in each cell during a given time-step. From this we can then generate random explosions across the dwarf galaxy. Note that, since the SFR of the simulation is tied to the dwarf's gas, the SNR is dependent on the amount of cold gas at that specific time-step, assuming that the SNe form and explode instantaneously. Using this method the SNR in a simulation of a dwarf in isolation (without the "coronal wind") is recovered within $\sim 10\%$ of the expected value [4].

[4] SNe alone are inefficient in removing the gas (see also §5.3). Thus, the SFR remains constant along the simulation and the simulated SNR can be compared with the predicted one. The match between the computed and the expected value (within 10%) shows the viability of our implementation.

3.5 Simulations setup

In Table 4 we list the details of our main runs. Different initial conditions for the dwarfs are computed by exploring the main model uncertainties: the orbit reconstruction, the determination of the SFH and the star formation law (see §4.2). Each set of runs for the two dwarfs has been simulated many times by changing the value of $n_{\rm cor}$ (which sets the dwarf's gas truncation radius $r_{\rm gas}$ and initial mass $M_{\rm gas}$ once the central gas density is fixed) until complete gas stripping occurs at the end of the simulation. We consider that a galaxy is devoid of gas when the mass of cold ($T < 1\times10^5$ K) gas bound to the potential of the dwarf is $< 5\%$ of the initial mass. The remaining small amount of cold gas can be easily stripped in the following part of the orbit. Large sizes of the computational box are needed to avoid boundary effects (such as reflected waves) on the surface of the dwarf. The boundaries used are "Wind" in the x-direction ("Inflow" on the right side and "Outflow" on the left one) and "Outflow" in the y-direction. The velocity of the inflow is set according to the selected orbits. Δr (and the corresponding Δt) is determined by the orbit's choice, and it represents the range of distances from the MW over which the recovered coronal density has effectively been averaged. Such values have been determined using equation (9) with a stripping efficiency of 50% (see §3.2).

4 RESULTS

In §4.1, we describe our fiducial simulation setup for Sextans, which has been obtained by taking the orbit with the median value of the pericentric distance $\bar{r}_{\rm p}$. For this fiducial setup, we illustrate the principal results of our analysis, in particular the procedure that we adopted to determine the coronal density (averaged over the distance range encompassed by the orbit) that produces complete stripping of the dwarf's ISM. We examine, in §4.2, how the estimate for the coronal density is affected by the choice of the orbit and the uncertainties in the initial conditions. In §4.3,

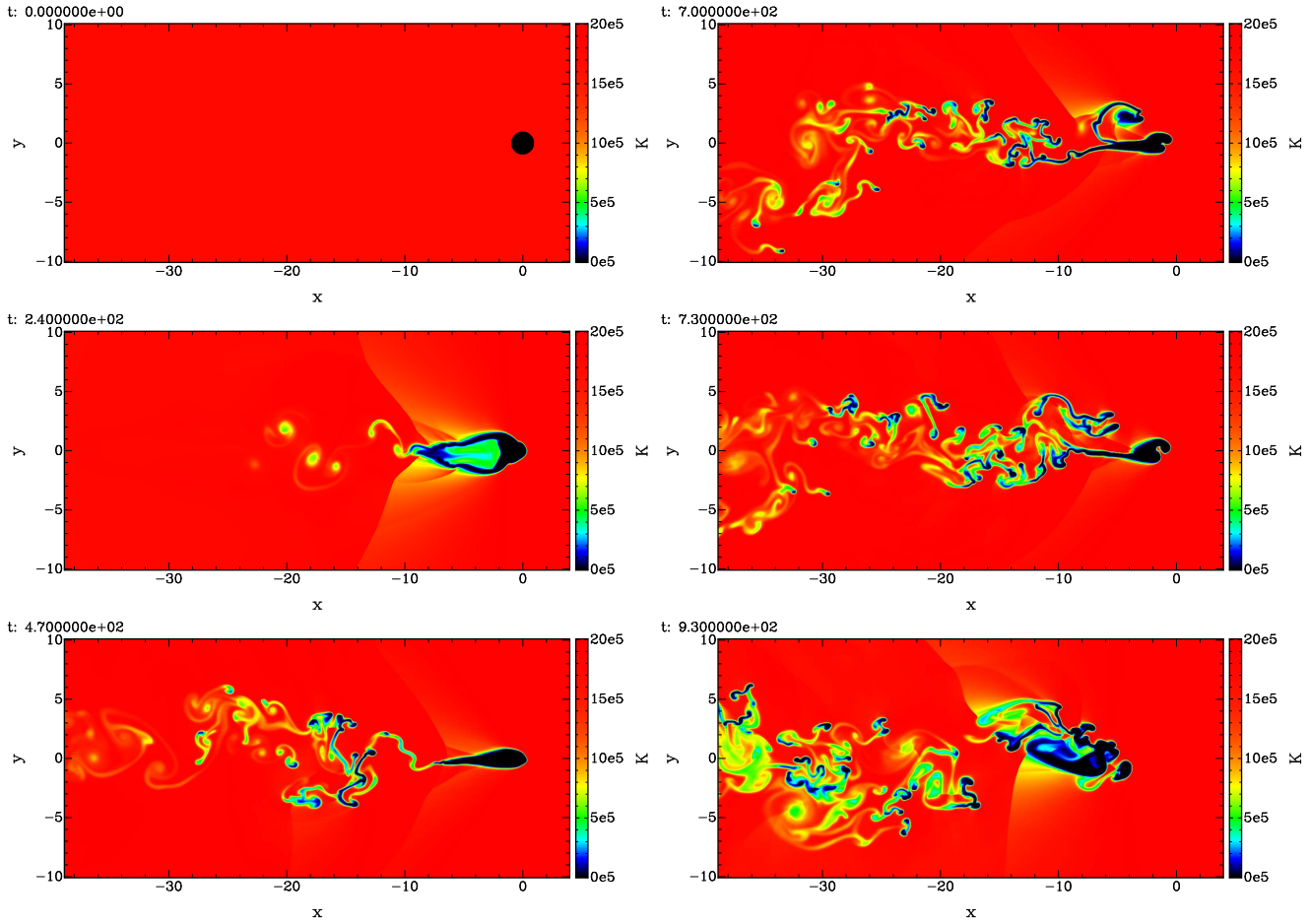

Figure 4. Time evolution of the temperature distribution for our fiducial setup for the Sextans dSph with $n_{\rm cor} = 1.8 \times 10^{-4}\,{\rm cm}^{-3}$. In the left column (top to bottom) we show $t = 0$, 240, and 470 Myr, and in the right column we plot $t = 700$, 730, and 930 Myr. The bottom left panel corresponds roughly to the time of pericentric passage. We only show a small section of the box. The axes are given in kpc.

we compare the values for the coronal density that we infer from Carina's simulations with those found for Sextans, and in §4.4 we show how the choice of different temperatures for the coronal gas affects the results.

4.1 Ram-pressure stripping from Sextans

We first examine the stripping of Sextans with the orbit parametrized by $\bar{r}_{\rm p} = 59.8\,{\rm kpc}$ (see §3.2) and all other parameters as quoted in Tables 1 and 2 and in the first line of Table 4, which represents our fiducial setup. We then run a series of simulations varying only the mean coronal density $n_{\rm cor}$ until we find the value that produces complete stripping of gas within the time of the simulation. We find that the minimum coronal density needed for stripping to occur is $n_{\rm cor}|_{\rm min} = 1.8 \times 10^{-4}\,{\rm cm}^{-3}$.

Fig. 4 shows the temperature distribution at times $t = 0, 240, 470, 700, 730, 930$ Myr. We see that, as the dwarf galaxy starts to experience the ram pressure exerted by the corona, a wake of stripped gas is formed. This wake becomes progressively more elongated and structured as time passes. In this wake knots of cold gas ($T \sim 10^4\,{\rm K}$) and regions at intermediate temperatures ($\sim 10^5\,{\rm K}$) co-exist. The presence of these intermediate temperature regions is indicative of a mixing between the stripped dwarf's ISM and the coronal material. The gas removal is not an instantaneous process. The mass loss rate is initially rather low and increases after the dwarf has passed the orbit pericentre. In Fig. 5, we show the evolution of the mass of the cold gas mass bound to Sextans (i.e. all gas with velocity less than the local escape velocity and $T < 10^5$ K). The mass of bound gas decreases steadily and at an increasing rate throughout the simulation. The increasing mass loss rate is a result of the progressive disruption of the dwarf by ram-pressure stripping assisted by SN feedback. Before the pericentre, only roughly 20% of the gas is lost, the other 80% is lost in the second half of the simulation. Approximately 1 Gyr is required to reach a final mass of cold, bound gas of $\sim 5 \times 10^4\,{\rm M}_\odot$, $\sim 1\%$ of the initial one.

4.2 Coronal gas density: lower bounds, errors and upper bounds

To reliably estimate the MW's coronal density, different sets of initial conditions must be explored to account for various uncertainties. The main model uncertainties are due to the orbit reconstruction, the determination of the SFH and the

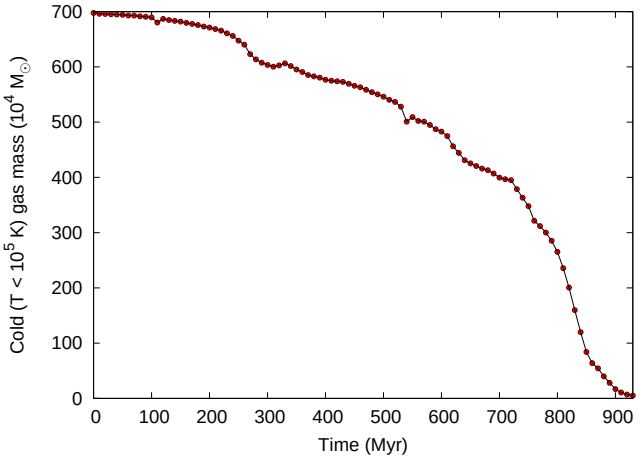

Figure 5. Mass of cold ($< 10^5$ K) gas gravitationally bound to the DM halo of Sextans as a function of time from the beginning of our fiducial simulation. The pericentre passage occurs at $t = 465$ Myr.

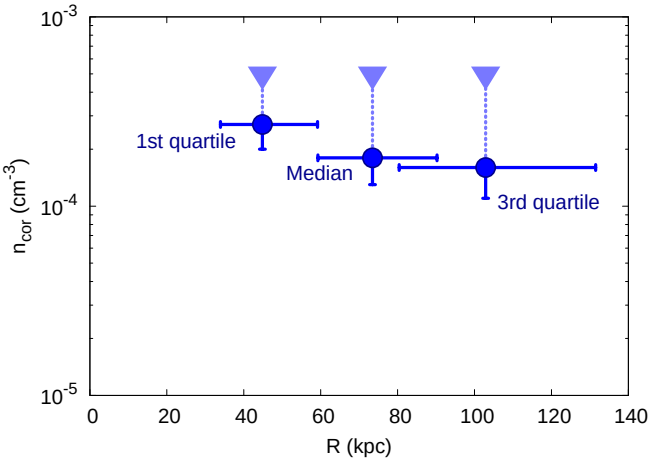

Figure 6. Density of the corona of the MW that produces complete gas stripping from the Sextans dSph. The different determinations refer to three representative orbits for the dSph with different pericentric radii, i.e. the median orbit, and the first and third quartiles of the distribution of pericentric radii. The down-pointing triangles show upper limits referred to that specific radius. The derivation of errors and upper limits is described in the text (§4.2).

star formation law. In this section, we consider in turn each of them.

We start with the uncertainties in the orbit determination. Fig. 6 shows the minimum values of the density of the MW's corona (points) that produce complete stripping from Sextans for the three representative orbits chosen in §3.2, i.e. the median value of $r_{\rm p}$ and the first and third quartiles of its distribution. The error bar in the radius represents the range over which the coronal density has to be considered average (see Table 4, eighth column, rows 1, 3, and 5, labelled as "mid"), while the derivation of the lower errors and the upper limits to the coronal density is described below. The orbital parameters used to derive the coronal densities shown in Fig. 6 are quite different (see Fig. 1 and §3.2). Nevertheless, the density required for the stripping is similar for the three orbits and shows a nice decreasing trend with the distance from the MW. This shows that the value of the coronal density is not too sensitive to the specific choice of the orbital parameters. The resulting values for $n_{\rm cor}|_{\rm min}$ are reported in Table 5 labelled as "mid".

Next we explore both the effect of the uncertainties on the measured SFH and on the applied star formation relation (equation (10)), which influence the value of initial gas density of the dwarf, $n_{0,\rm gas}$. To investigate the effect of a lower dwarf ISM density, we run an additional set of simulations (labelled as "low" in Tables 4 and 5). We derive the lower limit of the initial dwarf ISM density from an SFR of $2.4 \times 10^{-5}\,M_\odot{\rm yr}^{-1}$, corresponding to reducing the fiducial value of $4.6\times10^{-5}\,M_\odot{\rm yr}^{-1}$ by 1σ (see Table 2). We then use equation (10) with the upper +0.6 error to recover the lower $n_{0,\rm gas} = 0.18\,{\rm cm}^{-3}$, which is shown in rows 2, 4, 6 of Table 4. This gives a lower boundary for the coronal density which lies about 1σ below the fiducial value $n_{\rm cor} = 1.8\times10^{-4}\,{\rm cm}^{-3}$. These values represent the lower error bars in Fig. 6 for the different orbits.

The above gives us a *robust lower bound* on the hot corona density. As outlined in §2.2, we additionally use pressure equilibrium to estimate an upper bound $n_{\rm cor}|_{\rm max}$ by setting the gas truncation radius $r_{\rm gas}$ equal to the star formation radius $r_{\rm SF}$. In doing this, we are neglecting any conspicuous redistribution of stars after $t_{\rm lb}$. We plot the resulting upper limits as downward-pointing triangles in Fig. 6. Given the (large) uncertainties – particularly on the orbit of Sextans – it is quite remarkable that all the values of the coronal density derived here appear to be consistent with one another.

dSph point	$r_{\rm p}$ (kpc)	Δr (kpc)	$v_{\rm p}$ (km/s)	$\Delta t_{\rm lb}$ (Gyr)	$n_{\rm cor}\|_{\rm min}$ ($\rm cm^{-3}$)
Sextans					
mid	59.8	30.4	270.4	0.93	1.8×10^{-4}
low	59.8	30.4	270.4	0.93	1.3×10^{-4}
mid	33.9	25.3	333.6	0.42	2.7×10^{-4}
low	33.9	25.3	333.6	0.42	2×10^{-4}
mid	80.4	51.1	284.1	1.22	1.6×10^{-4}
low	80.4	51.1	284.1	1.22	1.1×10^{-4}
Carina					
mid	51.2	30.6	291.4	0.74	1.7×10^{-4}
low	51.2	30.6	291.4	0.74	1.5×10^{-4}

Table 5. Simulations that produced the complete stripping of gas from the dSphs. The labels "mid" and "low" refer to the initial density of the dwarf's ISM. $r_{\rm p}$ is the pericentre distance of the simulations, Δr is the considered spatial range from the pericentre found considering a stripping efficiency greater than 50% (see also Table 4), $v_{\rm p}$ is the velocity at the pericentre, $\Delta t_{\rm lb}$ is the simulation time and $n_{\rm cor}|_{\rm min}$ is the inferred *minimum* average coronal density needed for stripping.

4.3 Carina

We carry out a comparable set of simulations for the Carina dSph. For this dwarf we use only one orbit, i.e. that with median $r_{\rm p} = 51.2$ kpc, for which we find $n_{\rm cor}|_{\rm min} = 1.7 \times$

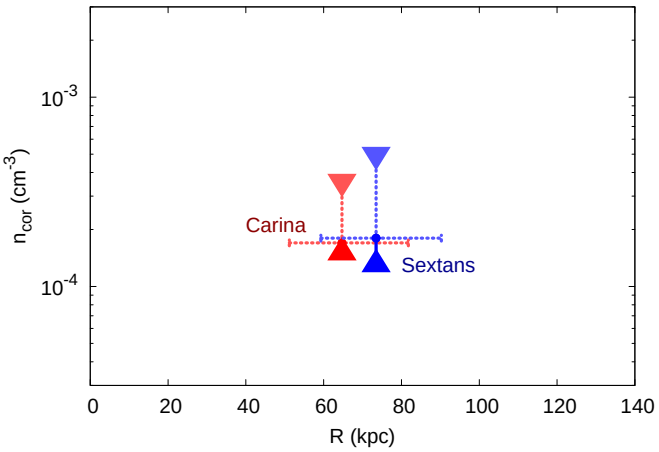

Figure 7. Ranges of gas densities of the MW's corona allowed by the Sextans (blue) and Carina (red) dwarfs. The derivation of the lower and upper bounds (triangles) is described in the text (§4.2).

$10^{-4}\,\mathrm{cm}^{-3}$. Estimating the lower error as before brings the lower limit down to $n_{\rm cor}|_{\rm min} = 1.5\times10^{-4}\,\mathrm{cm}^{-3}$ (Table 5).

We compare the coronal densities of the MW derived by using the median orbit of Sextans and Carina in Fig. 7. As in Fig. 6, the horizontal bar represents the range in radii that we have considered for the simulation. We now use upwards pointing triangles placed at the location of the lower 1σ error to denote our lower bound. The upper limits (downwards pointing triangles) are estimated with the method described in §4.2. The derived values for the coronal density are reported in Table 5, while in Table 6 we list the ranges of the radii and the upper and lower bounds of the coronal density obtained for the median orbits of Sextans and Carina. The two dSphs have rather different structural properties and orbital parameters (see again Tables 1, 2 and 4) and yet there is a remarkable consistency for the recovered density values in the range of radii in which the two orbits overlap. This fact further supports the basic soundness of the methodology that we adopt here. Note in particular that the times of the last stripping ($t_{\rm lb}$) for the two dwarfs are very different. This may be an indication that the density of the Galactic corona has not changed significantly in the last $\sim 7\,$Gyr. Note also that the assumption that there has been no significant redistribution of the stellar component within the dwarf should be fully justified for Carina where $t_{\rm lb}$ is only 0.5 Gyr.

As a final end-to-end test of our systematic error, we consider a pericentric passage at the peak of the SFH of Carina. By matching $\rho_{\rm gas}$ with the value extracted from the following bin of the SFH, we derive a Galactic corona density approximately three times larger than using $t_{\rm lb}$. It is possible that this systematic shift implies some evolution in Carina's orbit over time; this interpretation will be considered in more detail in a separate forthcoming paper. Here, we simply note that even this extreme test results in a systematic error that is comparable to our other uncertainties.

Radius (kpc)	range (kpc)	$n_{\rm cor}\|_{\rm min}$ (cm^{-3})	$n_{\rm cor}\|_{\rm max}$ (cm^{-3})
73.5	59.8-90.2	1.3×10^{-4}	5×10^{-4}
64.7	51.2-81.8	1.5×10^{-4}	3.6×10^{-4}

Table 6. Average density of the MW corona together with its upper and lower limits as derived from the ram-pressure stripping along the median orbits of Sextans and Carina.

4.4 Varying the coronal temperature

One of the main assumptions of our investigation is the temperature of the corona at the location of the dwarf galaxies. To study the effect of different coronal temperatures we run additional simulations using the median orbit of Carina with the same parameters used before but different $T_{\rm cor}$. In particular, we explore two additional coronal temperatures at $T_{\rm cor} = 3\times10^6$ and $1\times10^6\,$K. The corresponding results, averaged over the range $51 < r < 82\,$kpc from the MW, are $n_{\rm cor,3}|_{\rm min} = 1.5\times10^{-4}\,\mathrm{cm}^{-3}$ and $n_{\rm cor,1}|_{\rm min} = 2.5\times10^{-4}\,\mathrm{cm}^{-3}$. The increase (decrease) of the coronal temperature causes the density to be lower (higher) than our fiducial value. In §5.1, we discuss the implications of these results for the missing baryon problem.

5 DISCUSSION

5.1 Missing baryons and the MW's corona

The results for the coronal density necessary for the stripping of gas from Sextans and Carina are summarized in Table 6. Here we show a conservative lower bound (fiducial value − lower error) and the upper bound determined in §2.2. We conclude that the coronal density, being a monotonic decreasing function of R, averaged between 50 and 90 kpc must be in the range $1.3\times10^{-4} < n_{\rm cor} < 3.6\times10^{-4}\,\mathrm{cm}^{-3}$, consistent both with the detection claims by Gupta et al. (2012) and with the analytical estimates of Grcevich & Putman (2009). We recall that $n_{\rm cor}$ is the total gas density: $n_{\rm i}+n_{\rm e}$. The lower limit is computed by subtracting the average 1σ of Sextans and Carina lower values to the value of the coronal density ($n_{\rm cor} = 1.75\times10^{-4}\,\mathrm{cm}^{-3}$) determined by averaging our fiducial "mid" simulations (Table 5).

It is possible to use our derived range of $n_{\rm cor}$ as a constraint for the *global* density profile of the MW's corona. This profile is obtained by following the procedure outlined in §2.4. From the density profile one can extrapolate the total mass of the corona within the virial radius of the MW, which can then be compared to the missing baryonic mass of the Galaxy. In addition to $n_{\rm cor}$, we take also into account two further constraints discussed in AB10:

(i) the dispersion measures along the line of sight to Large Magellanic Cloud (LMC) pulsars, from which AB10 estimate an upper bound for the coronal density of $\overline{n}_{\rm e} = 5\times10^{-4}\,\mathrm{cm}^{-3}$ averaged over 50 kpc from the Galactic Centre;

(ii) the upper limit for X-ray emission measure, assuming our fiducial value of the coronal metallicity of 0.1 $Z_\odot$.

The dispersion measure of LMC pulsars is the more stringent

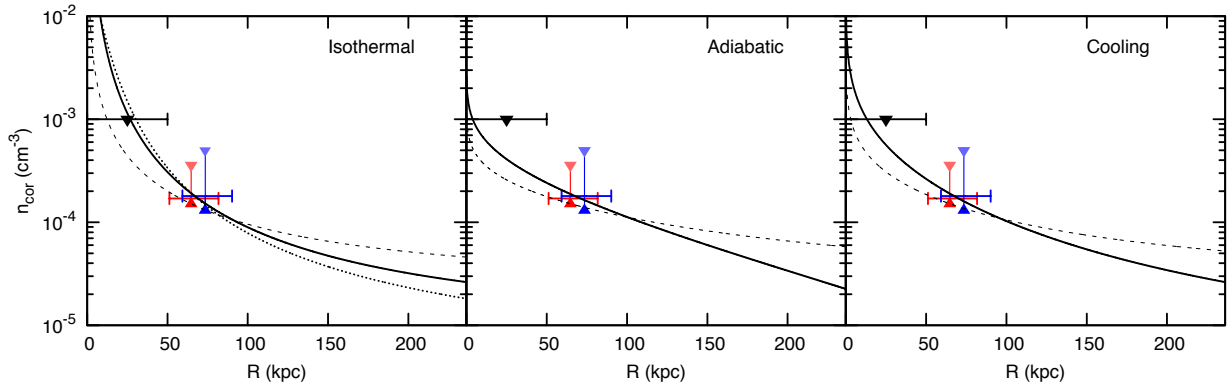

Figure 8. Density profiles for different coronal models consistent with all constraints: the range of coronal densities allowed by our analysis for Sextans and Carina, pulsar dispersion measures (black triangle) and X-ray emission upper limits (not shown). The solid line corresponds to $T_{\rm cor}(50-90\ {\rm kpc}) = 1.8\times10^6$ K and the dashed line to $T_{\rm cor}(50-80\ {\rm kpc}) = 3\times10^6$ K. The dotted line in the left-hand panel shows results for an NFW potential (as opposed to our default TF potential). From left to right, panels consider an isothermal ($\gamma = 1$), adiabatic ($\gamma = 5/3$), and 'cooling' ($\gamma = 1.33$) halo.

Potential	$T_{\rm cor}$	$\frac{M(<r_{\rm vir})}{M_{\rm mb}}$		$\frac{M(<r_{\rm vir})}{M_\odot}$	
-	(10^6 K)	Isothermal	Adiabatic	Isothermal	Adiabatic
TF	1.8	$15-20$ %	$16-48$ %	$3.6\times10^{10}-4.8\times10^{10}$	$3.8\times10^{10}-1.1\times10^{11}$
NFW	1.8	11 %	$9-25$ %	3.4×10^{10}	$2.8\times10^{10}-7.7\times10^{10}$
TF	3.0	$22-50$ %	$26-100$ %	$5.3\times10^{10}-1.2\times10^{11}$	$6.2\times10^{10}-2.4\times10^{11}$
NFW	3.0	$16-33$ %	$18-74$ %	$4.5\times10^{10}-10^{11}$	$5.6\times10^{10}-2.3\times10^{11}$

Table 7. The fraction and mass of the missing baryons contained in coronae for different combinations of coronal temperature, equation of state and Galactic potential consistent with the observational constraints.

constraint at present due to our assumption of a low coronal metallicity.

Through equation (6), we compute a series of coronal density profiles consistent with all of the above constraints, using three different assumptions about the thermodynamic state of the coronal gas: isothermal ($\gamma = 1$), adiabatic ($\gamma = 5/3$), and 'cooling' ($\gamma = 1.33$). As for the DM potential we make two different choices: our default TF potential (see equation (6) truncated at[5] 10 kpc $\leqslant R \leqslant R_{\rm vir} = 236$ kpc, with $M_{\rm vir} = 1.54\times10^{12}\,M_\odot$); and an NFW profile. We also consider three different coronal temperatures: 1.8×10^6, 10^6 and 3×10^6 K. The exploration of the parameter space resulted in 21 models compatible with all of the constraints considered here. In particular, we find that, regardless of the choice of the potential, for the isothermal models our upper limits are less stringent than the constraint from the dispersion measure, while for the adiabatic and cooling coronae they are roughly coincident. Hence, the upper limits on the MW's baryon fraction described in this section are determined by the dispersion-measure limit rather than our pressure-confinement method described in §2.2.

To derive the expected mass of the missing baryons $M_{\rm mb}$ associated with the Milky Way we follow again AB10 and set $M_{\rm mb} = 15\%\ M_{\rm tot}$, where $M_{\rm tot}$ is the sum of the DM mass ($M_{\rm vir}$) and the observed baryons mass. For the latter we take $M_{\rm ob} = 6\times10^{10}\,M_\odot$ (see §1). The expected missing baryon mass is then $2.4\times10^{11}\,M_\odot$ for the TF model.

Our results are presented in Fig. 8, where we show the ranges given by Sextans and Carina and the coronal profiles with reference values $n_{\rm cor} = 1.75\times10^{-4}$ and 1.5×10^{-4} cm^{-3} for $T_{\rm cor} = 1.8\times10^6$ and 3×10^6 K, respectively. All the models with $T_{\rm cor} = 10^6$ K yielded no solution consistent with all of the constraints and therefore are not shown. In the isothermal case, we find for $T_{\rm cor} = 1.8\times10^6$ K (3×10^6 K) a coronal baryon fraction of 15-20% (22-50%) of the expected MW's missing baryons, marginalizing over all uncertainties. For adiabatic and 'cooling' models instead, the temperature profile is no longer constant and so our assumed coronal temperature corresponds to an average over the ranges $50-90$ and $50-80$ kpc for $T_{\rm cor} = 1.8\times10^6$ and 3×10^6 K, respectively. The results for an adiabatic or 'cooling' halo are nearly indistinguishable, with a difference of $\lesssim 2\%$ in the recovered missing baryon fractions. For $T_{\rm cor}(50-90\ {\rm kpc}) = 1.8\times10^6$ K, we find a coronal baryon fraction of 16-48% of the expected missing baryons, while for $T_{\rm cor}(50-80\ {\rm kpc}) = 3\times10^6$ K the value is 26-100%. As expected, for an adiabatic or 'cooling' corona the baryon fraction can be significantly larger than in the isothermal case the density in such a corona drops less rapidly with radius, allowing more gas to be stored in the huge volume just inside the virial radius. An adiabatic corona at high temperature could, in principle, contain all of the MW's expected missing baryonic mass. These results are broadly consistent with those of AB10 and also the estimates of missing baryon fractions in external galaxies (Anderson & Bregman 2011; Dai et al. 2012; Anderson et al. 2013),

[5] This inner truncation is used to avoid any contamination from the disc and does not affect the value of the recovered coronal mass (see also AB10).

Point	$n_{\rm an}$ ($\rm cm^{-3}$)	$n_{\rm sim}$ ($\rm cm^{-3}$)	$\overline{n}_{\rm gas}$ ($\rm cm^{-3}$)	$\overline{v}_{\rm x}$ ($\rm km\,s^{-1}$)
Sextans				
Median	3.6×10^{-5}	1.8×10^{-4}	0.09	228
First quartile	2.3×10^{-5}	2.7×10^{-4}	0.09	286
Third quartile	3.1×10^{-5}	1.6×10^{-4}	0.09	246
Carina				
Median	3.2×10^{-5}	1.7×10^{-4}	0.14	251

Table 8. Comparison between the predicted values of the minimum coronal density for stripping from equation (12) (column 1) and the results of the "mid" simulations (column 2) listed in Tables 4 and 5 (see the text).

although our fractions are higher than theirs probably due to our lower value of the coronal metallicity.

Finally, we consider how our assumption of a TF profile affects these results. We use instead the NFW potential from AB10 with $R_{\rm vir} = 250\,\rm kpc$, $M_{\rm vir} = 2 \times 10^{12}\,M_\odot$ and concentration parameter $c = 12$ (see the dotted line, left-hand panel of Fig. 8). Notice that for an NFW profile, the gas density falls more steeply leading to a lower extrapolated total mass. However, the effect is typically quite small compared to the other uncertainties. Our results for the missing baryon fractions are summarized in Table 7. All isothermal models predict an amount of missing baryons in the corona between 10 and 50% of the expected value (see also Miller & Bregman 2013). If the hot gas has an adiabatic equation of state, the corona can accommodate more gas and we can not rule out that it could contain the whole predicted amount of missing baryons (see also Fang et al. 2013).

5.2 Comparison with the analytic ram-pressure stripping formula

We now compare the results of our simulations (Table 5) with the analytic estimates computed from equation (2). As in our simulations we approximate the motion of the dwarf through the corona as one-dimensional, the minimum coronal density averaged in the distance range Δr near the pericentre required to completely strip the gas away is

$$n_{\rm cor}|_{\rm min}(\Delta r) \sim \frac{\sigma_{\rm x}^2\ \overline{n}_{\rm gas}}{\overline{v}_{\rm x}(\Delta r)^2}\ , \qquad (12)$$

where $\overline{n}_{\rm gas}$ is the average gas density of the dwarf within $r_{\rm gas}$, $\overline{v}_{\rm x}(\Delta r)$ the average one-dimensional velocity of the dwarf ($v_{\rm x}(\Delta r)$=$v_{\rm r}(\Delta r)$ in our simulations) and $\sigma_{\rm x}$ the x-component of the central, isotropic stellar velocity dispersion. Table 8 presents our findings for the "mid" (fiducial) simulations listed in Tables 4 and 5. The analytic estimates have been obtained by considering $\sigma = 7.9$ and 6.6 $\rm km\,s^{-1}$ for Sextans and Carina, respectively (Walker et al. 2009). Our numerical results are greater by about a factor of 5 with respect to the analytic predictions of equation (12). For the first quartile orbit of Sextans, this difference reaches a factor of 10. We can conclude that over the small range of densities used here, the analytic formula for stripping does not give a fairly good estimate of the coronal density, leading to the conclusion that non-linear effects are fundamental in recovering realistic values of $n_{\rm cor}|_{\rm min}$.

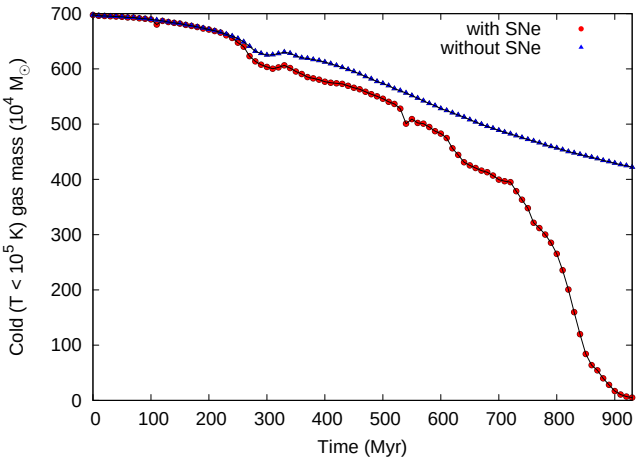

Figure 9. Cold, bound gas mass for the fiducial simulation of Sextans with and without SNe.

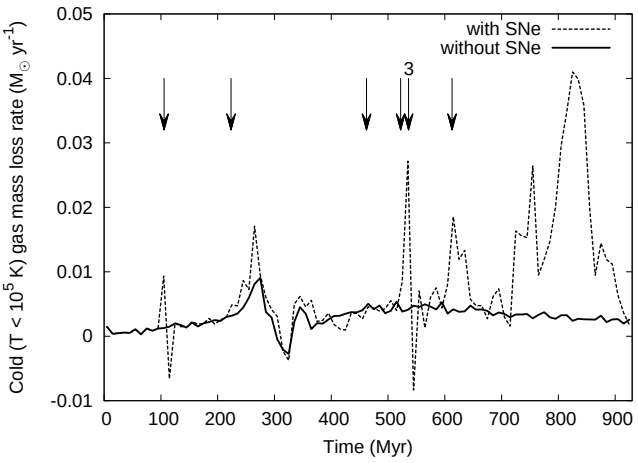

Figure 10. Cold gas mass loss rates for the fiducial simulation of Sextans with and without SNe. The arrows represent the time at which an SN has exploded; the number 3 over the fifth arrow means that a burst has occurred (three SNe in 8 Myr).

5.3 SN feedback

One of the novel features of this work is the introduction of discrete SN injections. If we do not consider SN explosions, the stripping process should naturally evolve towards a Kelvin-Helmholtz (KH) assisted regime. Additionally, the fact that we are using a varying dwarf velocity means that we expect the development of Rayleigh-Taylor (RT) instabilities. However, SN explosions are very efficient at changing the local morphology of the gas distribution, leading to an effective disruption of the RT/KH seeds. In practice, SNe destroy the regular flow at the interface between the hot and cold gas, leading to a SN-assisted stripping process. Without considering SN explosions, the gas flow past the dwarf is rather smooth and eddies form. Including SNe, as shown in Fig. 4, causes the flow to be quite clumpy. Perhaps, these cold clumps travelling at a few hundreds of $\rm km\,s^{-1}$ are re-

lated to (some of) the MW's HVCs (see also Mayer et al. 2006; Binney et al. 2009).

Figs 9 and 10 show the evolution of the cold bound mass and the cold mass loss rate for the fiducial simulation of Sextans (median orbit and $n_{\rm cor} = 1.8 \times 10^{-4}\,{\rm cm}^{-3}$) with and without SNe. SN explosions increase the cross-section of the cold gas distribution, leading to a more efficient stripping and a mass loss rate that can become four times larger than that without SNe (see Fig. 10). On the other hand, the same simulation including SNe but without ram-pressure stripping leads to an inefficient gas removal process, with a final cold gas mass very close to the initial one. For this reason, we conclude that it is the *combination* of SNe and ram pressure that is key for recovering the correct stripping rate. Without SNe, the coronal density required to completely strip away the gas is $n_{\rm cor}|_{\rm min} = 2.9 \times 10^{-4}\,{\rm cm}^{-3}$ – about two times higher than for our reference simulation with SNe. This is higher than independent observational limits on the coronal density (see §5.1), suggesting that SN explosions are critical for recovering realistic coronal profiles (see also Nichols & Bland-Hawthorn 2011).

6 CONCLUSIONS

We have performed a suite of hundreds of hydrodynamical simulations of ram-pressure stripping of two dwarfs, Sextans and Carina, in order to estimate a lower bound on the coronal gas density of the MW. In addition, we have derived an upper bound by considering the pressure confinement of these dwarfs by the hot corona. We have introduced several novel features as compared to previous analyses: realistic orbits for the dwarfs, a model of discrete SN feedback and a recovery of the initial gas mass contained in the dwarfs (determined from their measured SFHs). We find that the coronal number density in the range $50-90\,{\rm kpc}$ from the Galaxy must be in the range $1.3 \times 10^{-4} < n_{\rm cor} < 3.6 \times 10^{-4}\,{\rm cm}^{-3}$. We have considered many sources of systematic and random error ensuring that this result is robust.

We have derived coronal models consistent with our lower and upper bounds on the coronal density, X-ray emission limits, and pulsar dispersion measures. The pulsar constraint is particularly important in providing a more rigorous upper bound on the coronal density than our pressure confinement calculation (that requires an additional assumption about the radial extent of star formation within the dSphs). We have explored different coronal temperatures, Galactic potentials and equations of state for the gas, computing a set of coronal density profiles consistent with all of the above constraints. Extrapolating the baryonic mass in these models to large radii, we have estimated the fraction of 'missing baryons' that can exist in a hot corona within the MW's virial radius. Considering as a reference model an isothermal corona at $T_{\rm cor} = 1.8 \times 10^6\,{\rm K}$ in hydrostatic equilibrium with the Galactic potential, the missing baryon fraction is 10-20%. Hotter and/or adiabatic coronae can contain more baryons than our reference model. However, of the set of 21 coronal density profiles analysed in this work, only one model (hot and adiabatic) is consistent with all of the expected missing baryons lying within the virial radius of the MW. Thus, models for the MW must either explain why its corona is in a hot, adiabatic thermal state, or why a large fraction of the MW's baryons either never fell in, or were removed by energetic feedback.

ACKNOWLEDGEMENTS

We thank an anonymous referee for comments and suggestions that improved the clarity of this work. We also thank E. Held and L. Rizzi for providing data and M. Anderson, G. Battaglia, J. Binney, T. Naab, and S. White for helpful comments and discussions. We acknowledge the CINECA awards N. HP10CPPUNB and HP10C8MF3E (2011), the ETHZ Brutus Cluster and the RZG Odin Cluster for the availability of high performance computing resources and support. AG and SW thank the Deutsche Forschungsgemeinschaft (DFG) for funding through the SPP 1573 "The Physics of the Interstellar Medium". FF acknowledges support from PRIN-MIUR, project "The Chemical and Dynamical Evolution of the Milky Way and Local Group Galaxies", prot. 2011SPTACC. JIR would like to acknowledge support from SNF grant PP00P2_128540/1. FM is supported by the collaborative research centre "The Milky Way System" (SFB 881) of the DFG through subproject A1. HL acknowledges a fellowship from the European Commissions Framework Programme 7, through the Marie Curie Initial Training Network CosmoComp (PITN-GA-2009-238356). The original idea for this work arose during the inspiring meeting "Problematik" that took place at Magdalen College, Oxford (UK), in 2010 August.

REFERENCES

Anderson M. E., Bregman J. N., 2010, ApJ, 714, 320
Anderson M. E., Bregman J. N., 2011, ApJ, 737, 22
Anderson M. E., Bregman J. N., Dai X., 2013, ApJ, 762, 106
Anninos W. Y., Norman M. J., 1994, ApJ, 429, 434
Battaglia G., Helmi A., Tolstoy E., Irwin M., Hill V., Jablonka P., 2008, ApJL, 681, L13
Bigiel F., Leroy A., Walter F., Blitz L., Brinks E., de Blok W. J. G., Madore B., 2010, AJ, 140, 1194
Bigiel F., Leroy A. K., Walter F., Brinks E., de Blok W. J. G., Kramer C., Rix H. W., Schruba A., Schuster K.-F., Usero A., Wiesemeyer H. W., 2011, ApJL, 730, L13
Binney J., Merrifield M., 1998, Galactic Astronomy. Princeton University Press
Binney J., Nipoti C., Fraternali F., 2009, MNRAS, 397, 1804
Binney J., Tremaine S., 2008, Galactic Dynamics: Second Edition. Princeton University Press
Blitz L., Robishaw T., 2000, ApJ, 541, 675
Bregman J. N., 2007, ARA&A, 45, 221
Bregman J. N., Lloyd-Davies E. J., 2007, ApJ, 669, 990
Cole A. A., Skillman E. D., Tolstoy E., Gallagher III J. S., Aparicio A., Dolphin A. E., Gallart C., Hidalgo S. L., Saha A., Stetson P. B., Weisz D. R., 2007, ApJL, 659, L17
Combes F., Baker A. J., Schinnerer E., García-Burillo S., Hunt L. K., Boone F., Eckart A., Neri R., Tacconi L. J., 2009, A&A, 503, 73

Crain R. A., McCarthy I. G., Frenk C. S., Theuns T., Schaye J., 2010, MNRAS, 407, 1403
Dai X., Anderson M. E., Bregman J. N., Miller J. M., 2012, ApJ, 755, 107
de Blok W. J. G., Walter F., 2006, AJ, 131, 343
de Jong J. T. A., Harris J., Coleman M. G., Martin N. F., Bell E. F., Rix H.-W., Hill J. M., Skillman E. D., Sand D. J., Olszewski E. W., Zaritsky D., Thompson D., Giallongo E., Ragazzoni R., DiPaola A., Farinato J., Testa V., Bechtold J., 2008, ApJ, 680, 1112
Dehnen W., Binney J., 1998, MNRAS, 294, 429
Del Zanna L., Zanotti O., Bucciantini N., Londrillo P., 2007, A&A, 473, 11
Diaz J. D., Bekki K., 2012, ApJ, 750, 36
Dolphin A. E., 2000, ApJ, 531, 804
Dolphin A. E., Weisz D. R., Skillman E. D., Holtzman J. A., 2005, ArXiv Astrophysics e-prints
Efremova B. V., Bianchi L., Thilker D. A., Neill J. D., Burgarella D., Wyder T. K., Madore B. F., Rey S.-C., Barlow T. A., Conrow T., Forster K., Friedman P. G., Martin D. C., Morrissey P., Neff S. G., Schiminovich D., Seibert M., Small T., 2011, ApJ, 730, 88
Fang T., Bullock J., Boylan-Kolchin M., 2013, ApJ, 762, 20
Fossati M., Gavazzi G., Boselli A., Fumagalli M., 2012, A&A, 544, A128
Fukugita M., Peebles P. J. E., 2006, ApJ, 639, 590
Geha M., Blanton M. R., Masjedi M., West A. A., 2006, ApJ, 653, 240
Grcevich J., Putman M. E., 2009, ApJ, 696, 385
Guhathakurta P., Reitzel D. B., 1998, in Zaritsky D., ed., Galactic Halos Vol. 136 of Astronomical Society of the Pacific Conference Series, Local Group Suburbia: Red Giants in M31's Outer Spheroid and a Search for Stars in the Magellanic Stream. p. 22
Gunn J. E., Gott III J. R., 1972, ApJ, 176, 1
Gupta A., Mathur S., Krongold Y., Nicastro F., Galeazzi M., 2012, ApJL, 756, L8
Haan S., Schinnerer E., Mundell C. G., García-Burillo S., Combes F., 2008, AJ, 135, 232
Hodges-Kluck E. J., Bregman J. N., 2013, ApJ, 762, 12
Israel F. P., 1997, A&A, 328, 471
Kennicutt Jr. R. C., 1998a, ARA&A, 36, 189
Kennicutt Jr. R. C., 1998b, ApJ, 498, 541
Kepley A. A., Wilcots E. M., Hunter D. A., Nordgren T., 2007, AJ, 133, 2242
Klypin A., Zhao H., Somerville R. S., 2002, ApJ, 573, 597
Komatsu E., Dunkley J., Nolta M. R., Bennett C. L., Gold B., Hinshaw G., Jarosik N., Larson D., Limon M., Page L., Spergel D. N., Halpern M., Hill R. S., Kogut A., Meyer S. S., Tucker G. S., Weiland J. L., Wollack E., Wright E. L., 2009, ApJS, 180, 330
Kormendy J., 1985, ApJ, 295, 73
Krumholz M. R., Dekel A., McKee C. F., 2012, ApJ, 745, 69
Law D. R., Johnston K. V., Majewski S. R., 2005, ApJ, 619, 807
Lee M. G., Yuk I.-S., Park H. S., Harris J., Zaritsky D., 2009, ApJ, 703, 692
Leroy A. K., Walter F., Brinks E., Bigiel F., de Blok W. J. G., Madore B., Thornley M. D., 2008, AJ, 136, 2782
Li J.-T., Wang Q. D., 2013, MNRAS, 428, 2085
Lin D. N. C., Faber S. M., 1983, ApJL, 266, L21
Lux H., Read J. I., Lake G., 2010, MNRAS, 406, 2312
Marcolini A., Brighenti F., D'Ercole A., 2003, MNRAS, 345, 1329
Marinacci F., Binney J., Fraternali F., Nipoti C., Ciotti L., Londrillo P., 2010, MNRAS, 404, 1464
Marinacci F., Fraternali F., Nipoti C., Binney J., Ciotti L., Londrillo P., 2011, MNRAS, 415, 1534
Mastropietro C., Moore B., Mayer L., Wadsley J., Stadel J., 2005, MNRAS, 363, 509
Mateo M. L., 1998, ARA&A, 36, 435
Mayer L., Governato F., Kaufmann T., 2008, Advanced Science Letters, 1, 7
Mayer L., Mastropietro C., Wadsley J., Stadel J., Moore B., 2006, MNRAS, 369, 1021
McConnachie A. W., Venn K. A., Irwin M. J., Young L. M., Geehan J. J., 2007, ApJL, 671, L33
McGaugh S. S., Schombert J. M., de Blok W. J. G., Zagursky M. J., 2010, ApJL, 708, L14
Miller M., Bregman J., 2013, ArXiv e-prints
Moore B., Davis M., 1994, MNRAS, 270, 209
Mori M., Burkert A., 2000, ApJ, 538, 559
Nakanishi H., Sofue Y., 2006, PASJ, 58, 847
Navarro J. F., Frenk C. S., White S. D. M., 1997, ApJ, 490, 493
Nicastro F., Zezas A., Drake J., Elvis M., Fiore F., Fruscione A., Marengo M., Mathur S., Bianchi S., 2002, ApJ, 573, 157
Nichols M., Bland-Hawthorn J., 2011, ApJ, 732, 17
Nulsen P. E. J., 1982, MNRAS, 198, 1007
Pagel B. E. J., 1997, Nucleosynthesis and Chemical Evolution of Galaxies. Cambridge University Press
Pedersen K., Rasmussen J., Sommer-Larsen J., Toft S., Benson A. J., Bower R. G., 2006, New Astronomy, 11, 465
Planck Collaboration Ade P. A. R., Aghanim N., Armitage-Caplan C., Arnaud M., Ashdown M., Atrio-Barandela F., Aumont J., Baccigalupi C., Banday A. J., et al. 2013, ArXiv e-prints
Putman M. E., Saul D. R., Mets E., 2011, MNRAS, 418, 1575
Putman M. E., Staveley-Smith L., Freeman K. C., Gibson B. K., Barnes D. G., 2003, ApJ, 586, 170
Rasmussen J., Sommer-Larsen J., Pedersen K., Toft S., Benson A., Bower R. G., Grove L. F., 2009, ApJ, 697, 79
Read J. I., Gilmore G., 2005, MNRAS, 356, 107
Read J. I., Trentham N., 2005, Royal Society of London Philosophical Transactions Series A, 363, 2693
Read J. I., Wilkinson M. I., Evans N. W., Gilmore G., Kleyna J. T., 2006a, MNRAS, 367, 387
Read J. I., Wilkinson M. I., Evans N. W., Gilmore G., Kleyna J. T., 2006b, MNRAS, 366, 429
Rizzi L., Held E. V., Bertelli G., Saviane I., 2003, ApJL, 589, L85
Roediger E., Hensler G., 2005, A&A, 433, 875
Roychowdhury S., Chengalur J. N., Begum A., Karachentsev I. D., 2009, MNRAS, 397, 1435
Ryan-Weber E. V., Begum A., Oosterloo T., Pal S., Irwin M. J., Belokurov V., Evans N. W., Zucker D. B., 2008, MNRAS, 384, 535

Salpeter E. E., 1955, ApJ, 121, 161
Sarazin C. L., 2009, X-ray emission from Clusters of Galaxies. Cambridge University Press, Cambridge
Schmidt M., 1959, ApJ, 129, 243
Shull J. M., Smith B. D., Danforth C. W., 2012, ApJ, 759, 23
Spitzer Jr. L., 1956, ApJ, 124, 20
Strickland D. K., Heckman T. M., Colbert E. J. M., Hoopes C. G., Weaver K. A., 2004, ApJ, 606, 829
Sutherland R. S., Dopita M. A., 1993, ApJS, 88, 253
Taylor C. L., Klein U., 2001, A&A, 366, 811
Teyssier R., Pontzen A., Dubois Y., Read J. I., 2013, MNRAS, 429, 3068
Tolstoy E., Hill V., Tosi M., 2009, ARA&A, 47, 371
Wakker B. P., York D. G., Wilhelm R., Barentine J. C., Richter P., Beers T. C., Ivezić Ž., Howk J. C., 2008, ApJ, 672, 298
Walker M. G., Mateo M., Olszewski E. W., Peñarrubia J., Wyn Evans N., Gilmore G., 2009, ApJ, 704, 1274
Wilkinson M. I., Evans N. W., 1999, MNRAS, 310, 645
Yao Y., Nowak M. A., Wang Q. D., Schulz N. S., Canizares C. R., 2008, ApJL, 672, L21
Young L. M., Lo K. Y., 1996, ApJ, 462, 203